Optical Characterization of Two Cataclysmic Variables: RBS 0490 and SDSS J075939.79 +191417.3

Arti Joshi[1] , J. C. Pandey[2], Nikita Rawat[2], Ashish Raj[3], Wei Wang[1,4] , and H. P. Singh[3]

[1] School of Physics and Technology, Wuhan University, Wuhan 430072, People's Republic of China; wangwei2017@whu.edu.cn
[2] Aryabhatta Research Institute of Observational Sciences (ARIES), Nainital—263002, India
[3] Department of Physics and Astrophysics, University of Delhi, 110007 Delhi, India
[4] WHU-NAOC Joint Center for Astronomy, Wuhan University, Wuhan 430072, People's Republic of China

Abstract

We present optical photometric and spectroscopic observations of two cataclysmic variables (CVs), namely RBS 0490 and SDSS J075939.79+191417.3. The optical variations of RBS 0490 have been found to occur with a period of 1.689 ± 0.001 hr, which appears to be the probable orbital period of the system. Present photometric observations of SDSS J075939.79+191417.3 confirm and refine the previously determined orbital period as $3.14240928 \pm 0.00000096$ hr. The presence of long-duration eclipse features in the light curves of SDSS J075939.79+191417.3 indicates that eclipses might be due to an accretion disk and bright spot. The orbital inclination of SDSS J075939.79+191417.3 is estimated to be $\sim78°$ using the eclipse morphology. The phased light-curve variations during the orbital cycle of RBS 0490 provide evidence of emission from an independent second accretion region or a second fainter pole. Optical spectra of RBS 0490 and SDSS J075939.79+191417.3 show the presence of strong Balmer and weak He II ($\lambda 4686$) emission lines, along with the detection of strong Hβ emission lines with a large equivalent width. The characteristic features of RBS 0490 seem to favor low-field polars, while SDSS J075939.79+191417.3 appears to be similar to nonmagnetic systems.

Unified Astronomy Thesaurus concepts: Cataclysmic variable stars (203)

1. Introduction

Cataclysmic variables are semidetached close binary systems in which a white dwarf (WD) primary accretes material from the mass-donating secondary via Roche-lobe overflow (Warner 1995). The material transferred from the secondary flows through the inner Lagrangian point and orbits around the primary, forming an accretion disk in nonmagnetic systems. However, if the magnetic field strength of the WD is large enough, an accretion disk can form far from the WD, but the inner disk disrupts at the magnetospheric radius, and the field forces material to fall onto the poles of the WD. These systems have $P_\omega < P_\Omega$, where P_ω and P_Ω are spin and orbital periods respectively, and they are known as intermediate polars (IPs; Patterson 1994, and references therein). Alternatively, if the magnetic field of the WD is sufficiently strong, the magnetic pressure exceeds the ram pressure, preventing the formation of an accretion disk. The accreted matter follows the magnetic field lines of the WD and falls onto the poles (see Cropper 1990; Warner 1995). These binary systems are known as polars for which $P_\omega = P_\Omega$. The majority of polars have orbital periods shorter than the "period gap of 2–3 hr" (Scaringi et al. 2010). The optical and near-infrared radiation in these systems is dominated by cyclotron emission and originates from the accretion column near the WD in the post-shock region. These systems tend to show periodic modulation at the orbital period, and their optical spectra exhibit strong Balmer emission lines along with He I and He II emission lines (Warner 1986, and references therein). The Hβ and He II ($\lambda 4686$) emission lines are much stronger in polars and usually originate in the

accretion column. The majority of polars are single-pole accretors (e.g., Schwope et al. 1993; Salvi et al. 2002; Bridge et al. 2003), whereas some polars accrete onto both poles (e.g., Beardmore et al. 1995; Schwope et al. 1995; Schmidt et al. 1999) and others switch between single- and double-pole accretion (e.g., Rosen et al. 1996; Mason et al. 1998). In this paper, we present detailed analyses of two CVs, namely RBS 0490 and SDSS J075939.79+191417.3 (hereafter J0759) using the optical photometric and spectroscopic observations that were taken between the years 2005 and 2021.

RBS 0490 was detected during the ROSAT all-sky survey (RASS; Voges et al. 1999; Schwope et al. 2002) and found to be a ROSAT bright source. Inverting the Gaia parallax of RBS 0490 gives a distance of 320 ± 11 pc (Gaia Collaboration et al. 2021). Schwope et al. (2002) constructed a spectrum from 87 photons detected in the RASS and suggested that it can be modeled with a thermal bremsstrahlung component at a temperature of 20 keV. All emission lines appeared double-peaked in the optical spectrum of Schwope et al. (2002). Moreover, H Balmer and He I emission lines were very prominent, whereas He II emission lines were relatively weak. Later, Thorstensen et al. (2006) found a candidate radial-velocity period of 46 minutes. In contrast to Schwope et al. (2002), Thorstensen et al. (2006) found single-peaked emission lines, and only moderately strong He II $\lambda 4686$. Harrison & Campbell (2015) have analyzed the infrared data obtained from the Wide-field Infrared Survey Explorer (WISE) bands and suggested that it is a polar.

J0759 was identified as a CV by Szkody et al. (2006) based on the optical spectrum obtained during the Sloan Digital Sky Survey (SDSS). The SDSS spectrum shows strong Balmer emission (Hβ has an equivalent width (EW) of 72 Å), and an He II ($\lambda 4686$)/Hβ EW ratio of 0.2. Subsequently, they reported that J0759 reveals stronger He II ($\lambda 4686$) than most dwarf

Table 1
Log of Optical Photometric and Spectroscopic Observations of RBS 0490 and J0759

Object	Date of Observations	Facility	Instrument	Filter/ Band	Integration Time (s)	Time (JD$_t$)	Time Span (hr)
RBS 0490	2015 Oct 10	1.04 m—ST	1k × 1k CCD	R	300	2,457,305.00	3.52
	2015 Nov 6	1.3 m—DFOT	512 × 512 CCD	R	200	2,457,333.00	3.87
	2017 Dec 22	2.01 m—HCT	HFOSC/Gr7	380–780 nm	3600	2,458,110.08	1.00
	2018 Nov 30	2.01 m—HCT	HFOSC/Gr7	380–780 nm	3000	2,458,453.27	0.83
J0759	2016 Mar 7	1.3 m—DFOT	512 × 512 CCD	R	300	2,457,455.00	4.11
	2021 Feb 6	1.3 m—DFOT	2k × 2k CCD	R	300	2,459,252.00	3.49
	2021 Feb 7	1.3 m—DFOT	2k × 2k CCD	R	300	2,459,253.00	3.40
	2021 Feb 8	1.3 m—DFOT	2k × 2k CCD	R	300	2459,254.00	3.52
	2021 Feb 15	1.04 m—ST	4k × 4k CCD	R	300	2,459,261.00	3.24
	2018 Dec 17	2.01 m—HCT	HFOSC/Gr7	380–780 nm	3600	2,458,470.39	1.00
	2019 Feb 9	2.01 m—HCT	HFOSC/Gr7	380–780 nm	3600	2,458,524.36	1.00
	2020 Jan 14	2.01 m—HCT	HFOSC/Gr7	380–780 nm	2700	2,458,863.45	0.75
	2021 Mar 31	2.01 m—HCT	HFOSC/Gr7	380–780 nm	3600	2,459,305.08	1.00
	2021 Apr 24	2.01 m—HCT	HFOSC/Gr7	380–780 nm	3600	2,459,329.10	1.00

Note. JD$_t$ for HFOSC is the start time of the observations, whereas for photometric observation it is observation day.

novae but not quite up to the values typical for polars or IPs. Later, Gänsicke & Dillon (2009) reported an orbital period of ~188.45 minutes for J0759 using the SDSS spectroscopy. However, a much refined period of 0.1309337 day is reported in the AAVSO VSX catalog based on the data obtained from the Catalina Real-time Transient Survey (CRTS) and Zwicky Transient Facility (ZTF). Using the Gaia parallax (Gaia Collaboration et al. 2021), the distance of J0759 is calculated to be 1873 ± 535 pc.

The paper is organized as follows. We summarize the description of observations and data reduction in the next section. Analyses and the results of the optical data are described in Section 3. Finally, we present discussion and conclusions in Sections 4 and 5, respectively.

2. Observations and Data Reduction

2.1. Optical Photometric Observations

R-band photometric observations of both sources were carried out during the years 2015, 2016, and 2021 using the 1.04 m Sampuranand Telescope (ST; Sinvhal et al. 1972) and 1.3 m Devasthal Fast Optical Telescope (DFOT; Sagar et al. 2011) of ARIES, Nainital, India. A detailed log for photometric observations is given in Table 1. The ST was equipped with a 1k × 1k CCD and 4k × 4k CCD during observations of epochs 2015 and 2021, respectively. However, the DFOT was equipped with CCDs of 2k × 2k during the epoch 2021 and 512 × 512 during observations of epochs 2015 and 2016. Several bias and twilight sky flat frames were also acquired during each observing run. Preprocessing of each observed frame was performed using IRAF[6] software. To obtain the instrumental magnitudes, differential photometry in the manner of variable minus comparison star was performed by using a comparison star in the same field. The details of the adopted comparison stars labeled "C1" and "C2" for each source are given in Table 2. The constant brightness of comparison stars was checked by inspecting the light curves of "C1–C2" for each source separately. For consecutive epochs of observation (see Table 1), the nightly means of the standard deviation of "C1–C2" were derived as 0.0052 and 0.0045 for RBS 0490,

Table 2
Comparison Stars Used for the Differential Photometry for RBS 0490 and J0759

Object	Reference USNO-B1.0	B1 (mag)	R1 (mag)	B2 (mag)	R2 (mag)
RBS 0490	0731–0063800	16.89	16.53	18.30	17.11
"C1"	0731–0063769	15.20	13.96	15.26	14.12
"C2"	0731–0062447	16.63	14.66	16.95	15.40
J0759	1092–0155844	18.26	18.50	18.65	17.84
"C1"	1092–0155866	16.81	15.78	16.79	15.63
"C2"	1092–0155859	17.13	15.73	16.94	15.65

Note. C1 and C2 stand for comparisons 1 and 2 for each program star.

and 0.0055, 0.0024, 0.0040, 0.0040, and 0.0091 for J0759. Finally, the R-band magnitudes of observations were computed with respect to comparison star "C1."

2.2. TESS, ZTF, and CRTS Observations

RBS 0490 was observed by the Transiting Exoplanet Survey Satellite (TESS) with camera 2 in sector 31 for 25 days at a two-minute cadence from 2020 October 22 to November 16. TESS was launched on 2019 April 18 into a 13.7 days orbit. It has four small telescopes with four cameras and each has a field of view of 24×24 deg^2. They are aligned to cover $24 \times 90°$ strips of the sky called "sectors" (see Ricker et al. 2015, for details). The TESS bandpass extends from 600 to 1000 nm with an effective wavelength of 800 nm. TESS observations of RBS 0490 were continuous except for a gap of ~56.8 hr halfway into the sector. The data from RBS 0490 were stored in the Mikulski Archive for Space Telescopes (MAST) data archive with identification number "TIC 279483438." Data taken during an anomalous event had quality flags greater than 0 in the FITS file data structure and thus we have considered only the data with "QUALITY flag" = 0. We have taken values of PDCSAP flux, which is the simple aperture photometry flux after correction for systematic trends common to all stars.

The ZTF is a northern-sky synoptic optical survey for high-cadence time-domain astronomy, which used the Palomar 48 inch (P48) telescope (Bellm et al. 2019; Graham et al. 2019; Dekany et al. 2020). Its CCD camera consists of 16 6k × 6k

---

[6] IRAF is distributed by the National Optical Astronomy Observatories, USA.

E2V CCDs, producing a 47 deg^2 field of view. There are three available filters: ZTF-g, ZTF-r, and ZTF-i. Exposure times are usually 30 s for the g and r bands and 60 s for the i band. RBS 0490 and J0759 were observed by ZTF between 2018 and 2021. ZTF lists a total of 339 exposures for RBS 0490 from 2018 September 23 to 2021 February 26 and 520 exposures for J0759 from 2018 March 28 to 2021 April 24.

J0759 was also observed by the CRTS (Drake et al. 2009, 2014) between 2005 April 9 and 2013 December 24 in the V-filter. CRTS combines three distinct surveys—the Mount Lemmon Survey (MLS) and the Catalina Schmidt Survey (CSS) in the Northern Hemisphere and the Siding Spring Survey (SSS) in the South. The CRTS data for J0759 are available from the MLS and CSS surveys, and it's light curves are easily accessible online.

2.3. Optical Spectroscopic Observations

We obtained long-slit low-resolution optical spectra of both sources from the year 2017 to 2021 using the 2.01 m Himalayan Chandra Telescope at IAO, Hanle which is equipped with the Hanle Faint Object Spectrograph and Camera (HFOSC; Prabhu & Anupama 2010). A detailed log of the spectroscopic observations is given in Table 1. For all epochs, the observations were taken using the grism Gr7 (3800–7800 Å) with a resolution of 1330 and dispersion of 1.45 Å pixel^{-1}. Spectrophotometric standard stars were also observed during each observing run. The three main steps in data reduction of the standard and program stars were accomplished using IRAF tasks: preprocessing, wavelength calibration, and flux calibration. Lamp spectra of Fe–Ar were used for the wavelength calibration. The night sky emission lines at 5577 Å, 6300 Å, and 6363 Å were used to check the appropriate shift, and the shift was then applied with the SPECSHIFT task wherever it was required.

3. Analysis and Results

3.1. RBS 0490

3.1.1. Light-curve Morphology and Power Spectra

Figure 1(a) combines the TESS, ZTF-r/g, and our own R-band observations of RBS 0490 from the years 2015–2021. To probe RBS 0490 in more detail, we have closely inspected its light curve observed from each facility independently. The full TESS light curve of RBS 0490 and a zoomed-in version of its one-day observations are shown in Figure 1(b), whereas the R-band light curves are shown in Figure 1(c). Its light-curve variations are associated mostly with the bright maxima along with minima and exhibit the periodic nature of the system. This periodic nature has been demonstrated by applying the Lomb–Scargle (LS) periodogram algorithm (Lomb 1976; Scargle 1982; Horne & Baliunas 1986) to the entire TESS, ZTF-r, and R-band observations. The LS power spectrum obtained from the TESS data for RBS 0490 is shown in the top panel of Figure 2. The observed highest significant peak in the TESS power spectrum corresponds to a period of 1.689 ± 0.001 hr and is found to lie above the 99% confidence level. The significance of this detected peak is determined by calculating the false alarm probability (Horne & Baliunas 1986). The confidence level is represented by the dotted red lines. In contrast to radial-velocity measurements of Thorstensen et al. (2006), we have not detected any significant period near

46 minutes. We provisionally identify the 1.689 hr period with P_Ω.

From the R-band photometric data, we have detected a significant period of 1.689 ± 0.001 hr, which is identical to the period derived from the TESS data. The LS power spectrum obtained from the photometric data is shown in the middle panel of Figure 2. The ZTF-r-band light curve of RBS 0490 is very sparse and resulted in a noisy power spectrum as shown in the bottom panel of Figure 2. The orbital frequency obtained from the ZTF data is also marked in this figure. The significant periods derived from the LS photometric, TESS, and ZTF data are given in Table 3.

3.1.2. Orbital-Phased Light-curve Variations and System's Geometry

We explored the phased light-curve variation of RBS 0490 during its binary motion. Light curves obtained from the TESS and R-band observations are folded using the time of first observation, JD = 2,457,305.572836, as the reference epoch. However, the sparse light curve spanning several years in the ZTF-r-band is not useful for producing meaningful phase-dependent light-curve variations. Phase-folded light curves with phase bins of 0.0222 and 0.05 for TESS and R-band observations, respectively, are shown in Figure 3. Although the R-band light curve is less extensive, both TESS and R-band light curves appear to show almost consistent light-curve variations. However, a careful inspection of the phased light curve from the TESS observations shows double-humped-like features that are separated by an orbital phase of 0.5, whereas the phased R-band light curve shows a plateau-like structure followed by a broad hump.

Using the mean empirical mass–period relation given by Smith & Dhillon (1998), we have derived the mass and radius of the secondary as $0.10(\pm 0.02)\ M_\odot$ and $0.16(\pm 0.01)\ R_\odot$, respectively. Using an orbital period of 1.689 hr, we have estimated the mean density of the secondary, $\bar{\rho} = 36.8\ \mathrm{g\,cm}^{-3}$ (see Warner 1995, for formulae), which corresponds to a lower main-sequence star of spectral class M5.6 and an effective temperature of 2975 K (see Beuermann et al. 1998; Knigge 2006). Using the mass range of WDs of $0.2-1.5\ M_\odot$ in CVs (Zorotovic et al. 2011), the binary separation (a) is estimated to be in the range $(3.3-5.8) \times 10^{10}$ cm.

3.1.3. Optical Spectroscopy

Optical spectra with a wealth of spectral features were observed for RBS 0490 during two different epochs of observation. Figure 4 shows the optical spectra of RBS 0490 for epochs 2017 December 22 and 2018 November 30. Identification, flux, EW, and FWHM of the principal emission lines of RBS 0490 obtained through a single-Gaussian fitting are given in Table 4. Optical spectra of RBS 0490 exhibit a flat continuum and strong Balmer emission lines (from Hα to Hζ), He I, and He II emission lines. The He II λ4686 line is only modestly strong. The observed spectra resemble the spectra of Schwope et al. (2002) and Thorstensen et al. (2006) observed during epochs 1997, 1998, and 2002. Similar to Thorstensen et al. (2006), we observed all the spectral lines as single-peaked, whereas Schwope et al. (2002) describes them as being double-peaked. The values of flux and EW are found to be variable during the present and previous epochs of observation (see Schwope et al. 2002; Thorstensen et al. 2006, and present work).
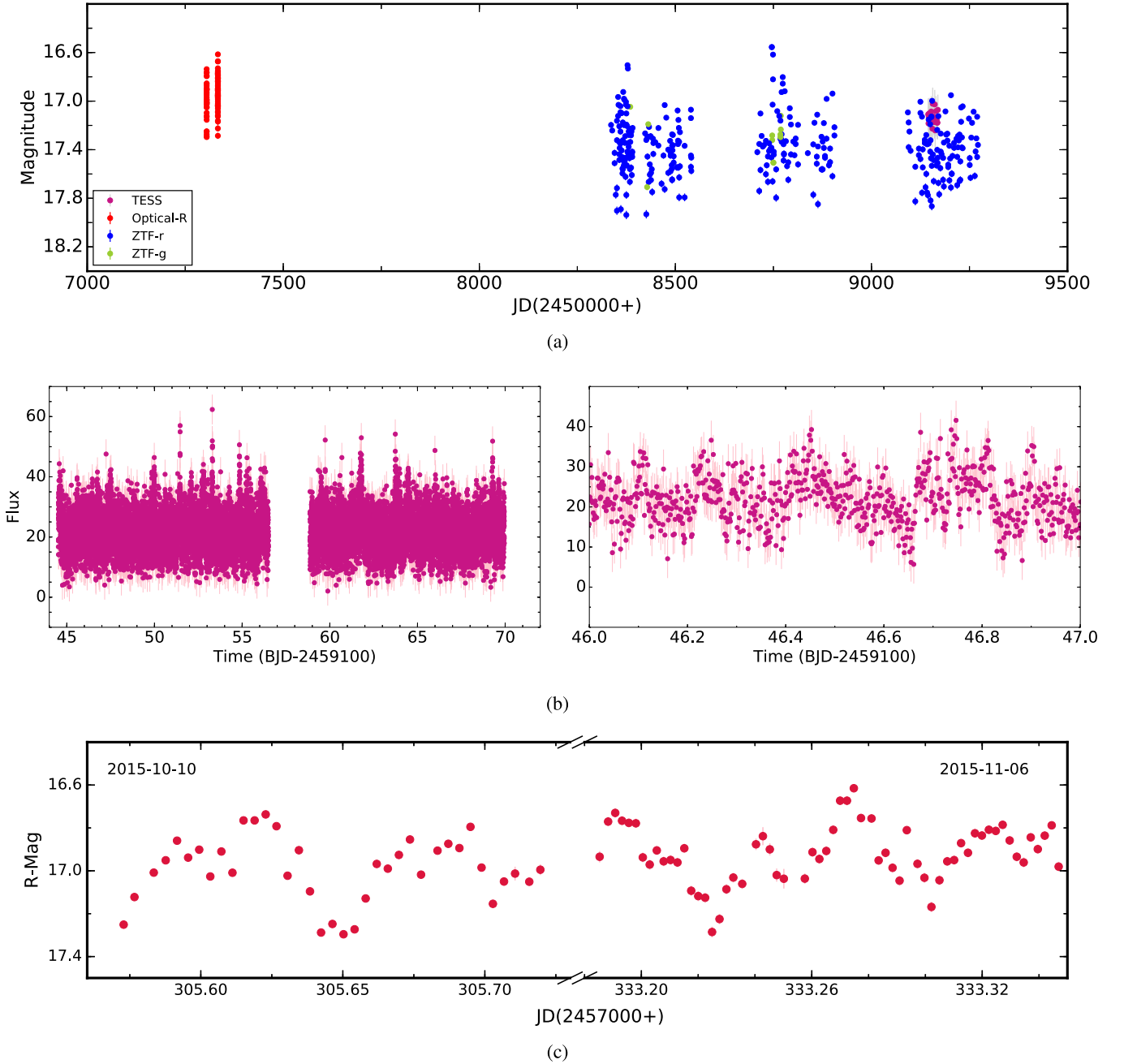
Figure 1. (a) Combined *R*-band, TESS, and ZTF-*r/g* light curves of RBS 0490, (b) the full TESS light curve of RBS 0490, where the right panel shows a zoomed-in version of the one-day observation, and (c) *R*-band light curves of RBS 0490 for two epochs of observation.

3.2. SDSS J075939.79+191417.3

3.2.1. Light-curve Morphology and Power Spectra

Figure 5 shows complete CRTS, *R*-band, and ZTF-*r/g* light curves of J0759 where the variable nature of the source is clearly evident. *R*-band data from the epoch 2021 are found to be observed simultaneously with a few epochs of ZTF in the *r* and *g* bands. To probe the system deeply, we have further inspected the temporal properties of J0759 from the CRTS, *R*-band, and ZTF-*r/g* band observations separately. We have obtained a total of 17.76 hr of photometric data from our observations carried out over five nights. *R*-band light curves for five epochs of observation are shown in Figure 6. The light curves of J0759 exhibit a clear eclipse profile with an average

dip of ∼2 mag and eclipse duration of ∼40 minutes. Successive eclipses spaced by ∼3.1 hr were observed on two of the five nights. Similar to the *R*-band light curve, the ZTF observations of J0759 also reveal the eclipse profiles in their light curves where the brightness drops by ∼2.0 mag as seen in the *R*-band light curve. A complete eclipse profile is seen in the ZTF-*r*-band light curve for the epoch 2019 December 10, which is shown in the second panel of Figure 6.

In order to find the periodicity from the eclipsed light curves of J0759, we have applied a phase dispersion minimization (PDM; Stellingwerf 1978) algorithm to the combined photometric, ZTF, and CRTS observations. Because of the large data gap between epochs 2016 and 2021, we have used combined photometric data observed during the epoch 2021 for
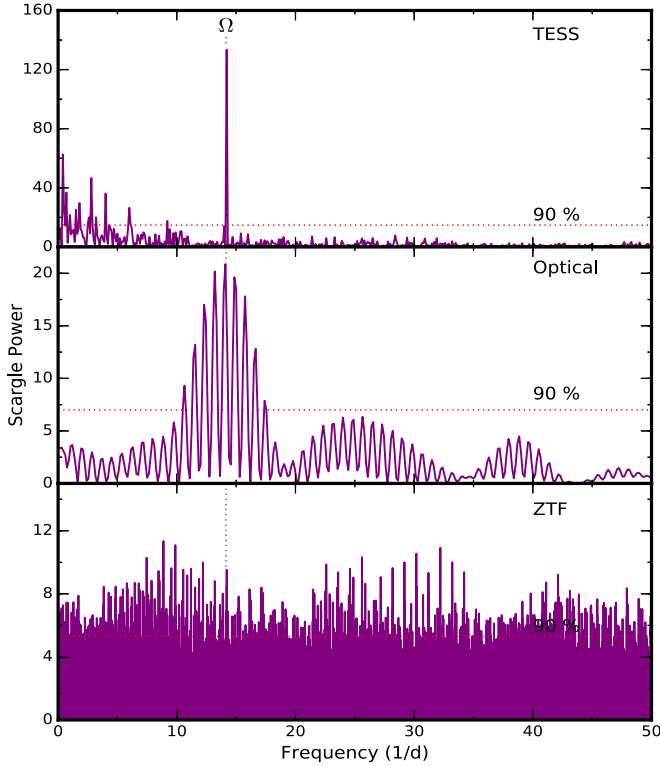
Figure 2. The Lomb–Scargle power spectra of RBS 0490 obtained from the complete data set of the TESS, *R*-band, and ZTF-*r*-band observations. The horizontal dotted lines in the Lomb–Scargle power spectra represent the 90% confidence level.

squares fit to these eclipse timings yields

$$T_0 = \text{JD } 2{,}457{,}455.16054(45) \pm 0.13093372(4)E, \qquad (1)$$

where T_0 is defined as the time of mid-eclipse, E is the cycle number, and the errors are given in brackets. The orbital period is thus derived to be $3.14240928 \pm 0.00000096$ hr. We have also folded the ZTF-*r*-band light curve of the epoch 2019 December 10 and *R*-band light curves using ephemeris as derived in Equation (1). Figure 8 shows the orbital-phase-folded light curves of J0759. Each light curve of J0759 reveals a deep eclipse profile with variable brightness. We have also found evidence of a secondary eclipse near phase 0.5 during all epochs of observation with approximate depths in the range 0.14–0.3 mag. We could not see any eclipse around phase 0.5 in the ZTF-*r*-band light curve due to its sparse phase coverage.

Using the eclipse width at half depth $(\Delta\phi)$, we derive the orbital inclination of the binary system by using the equation given by Eggleton (1983):

$$\left(\frac{R_2}{a}\right)^2 = \sin^2(\pi\Delta\phi) + \cos^2(\pi\Delta\phi)\cos^2 i, \qquad (2)$$

where R_2/a depends only on the mass ratio as

$$\frac{R_2}{a} = \frac{Cq^{2/3}}{Dq^{2/3} + \ln(1 + q^{1/3})}. \qquad (3)$$

The coefficients C and D are given by Eggleton (1983) as 0.49 and 0.6, respectively, for a spherical shape of the Roche lobe. However, in the case of CVs, the Roche lobe of the secondary

Table 3
Periods Corresponding to Dominant Peaks in the Power Spectra of RBS 0490 and J0759 Obtained from the *R*-band Photometry, TESS, ZTF, and CRTS Observations

| Period (hr)	*R*-band Photometry	TESS/CRTS[a]	ZTF
		RBS 0490	
P_Ω	1.6894 ± 0.0011	1.6894 ± 0.0012	1.6895 ± 0.0003
		J0759	
P_Ω	3.149025 ± 0.011338	3.142396 ± 0.000032	3.142387 ± 0.000092
$P_{2\Omega}$	1.573160 ± 0.002824	1.571206 ± 0.000008	1.571194 ± 0.000023
$P_{3\Omega}$	1.054452 ± 0.001268	1.047469 ± 0.000004	1.047473 ± 0.000010
$P_{4\Omega}$	0.789414 ± 0.000711	0.789678 ± 0.000002	0.785603 ± 0.000006

Note.
[a] Period obtained from TESS data for RBS 0490 and from CRTS data for J0759.

periodogram analysis. The PDM power spectra of *R*-band, ZTF, and CRTS data are shown in Figure 7. Various prominent peaks are found in the PDM power spectra. The first prominent peak in the PDM periodogram of photometric, ZTF, and CRTS data corresponds to the orbital period of ∼3.1 hr and perfectly matches with the time span where the primary eclipse completes its one cycle (see Figure 6). Other peaks are also observed in the PDM power spectra and correspond to harmonics of the orbital frequencies.

3.2.2. Orbital-phased Light-curve Variations and the System's Geometry

We have determined a total of seven mid-eclipse timings (see Table 5) by fitting a Gaussian function to the bottom part of eclipses. Only those epochs of observation were used for which complete eclipse profiles were observed. A linear least-

is not spherical, being largest size as "seen" from the WD and smallest in the polar direction. Therefore, we have used the coefficients $C = 0.4990$ and $D = 0.5053$ (Andronov & Andrych 2014). Further, using the same approach as described in Section 3.1.2, the mass and radius of the secondary are estimated as $0.28(\pm0.01)\ M_\odot$ and $0.33(\pm0.01)\ R_\odot$, respectively. Assuming the minimum and maximum values of WDs in CVs of 0.2 $M_\odot$ and 1.5 $M_\odot$, the limiting values of q are estimated as 1.4 and 0.19, respectively. For each consecutive epoch of *R*-band observations (see Table 1) and ZTF-*r*-band observations of the epoch 2019 December 10, the eclipse width at half depth $(\Delta\phi)$ was estimated as 0.081 ± 0.003, 0.077 ± 0.004, 0.078 ± 0.005, 0.082 ± 0.004, 0.068 ± 0.005, and 0.087 ± 0.004. Adopting the average values of $\Delta\phi$ and q of 0.079 ± 0.002 and 0.35 (assuming the average value of the mass of WDs in CVs as 0.8 $M_\odot$; Zorotovic et al. 2011),
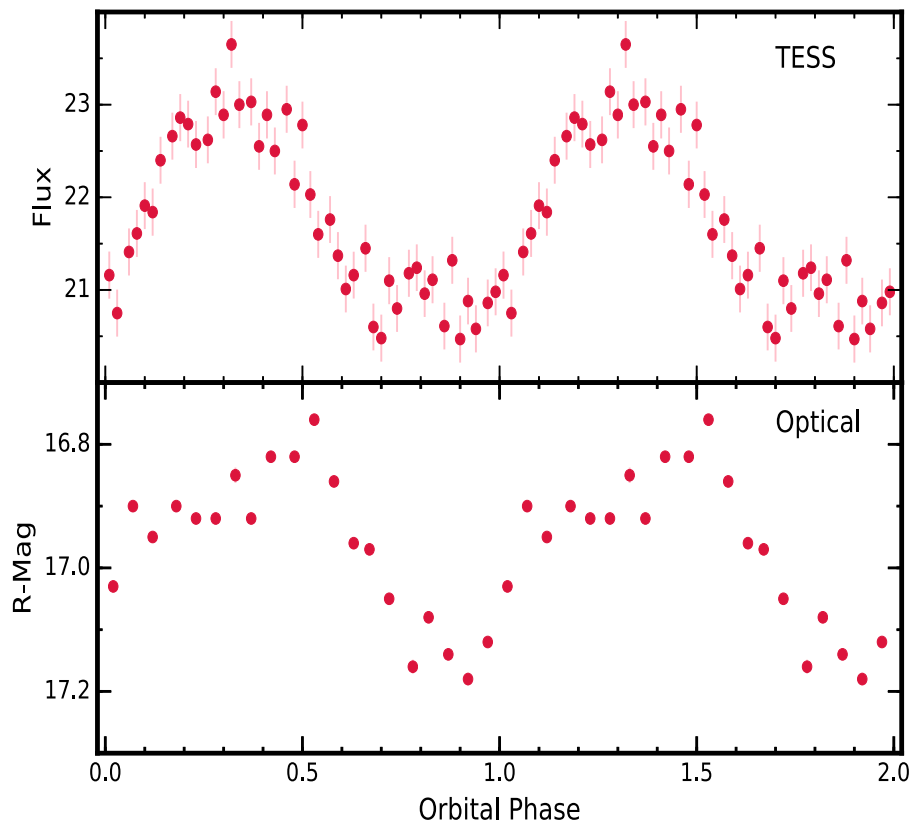
Figure 3. Orbital-phase-folded light curves of RBS 0490 obtained from the TESS and *R*-band observations with phase bins of 0.0222 and 0.05, respectively.
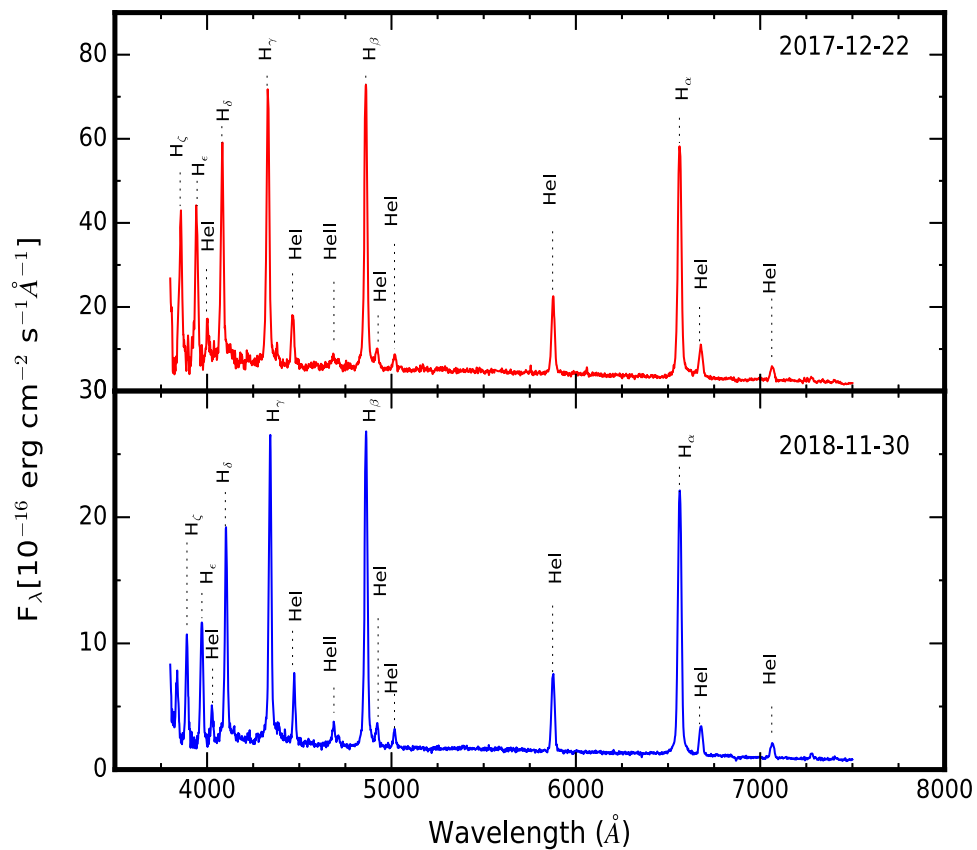

Figure 4. Optical spectra of RBS 0490 for two epochs of observation as mentioned in each panel.

respectively, the orbital inclination (*i*) is estimated to be ∼78°.

Table 4
Identification, Flux, EW, and FWHM for Emission Features in the Spectra of RBS 0490 and J0759

| Identification | RBS 0490 | | | | | | J0759 | | | | | | | | | | | | | | |
| | 2017-12-22 | | | 2018-11-30 | | | 2018-12-17 | | | 2019-2-9 | | | 2020-1-14 | | | 2021-3-31 | | | 2021-4-24 | | |
	Flux	−EW	FWHM	Flux	−EW	FWHM	Flux	−EW	FWHM	Flux	−EW	FWHM	Flux	−EW	FWHM	Flux	−EW	FWHM	Flux	−EW	FWHM
Hζ (3889 Å)	126	54	1123	705	108	1535	...	...	...	...	...	...	...	...	...	...	...	...	...	...	...
Hε (3970 Å)	182	98	1318	696	109	1390	...	...	...	...	...	...	...	...	...	...	...	...	...	...	...
He I (4026 Å)	40	18	1094	150	20	1250	...	...	...	...	...	...	...	...	...	...	...	...	...	...	...
Hδ (4102 Å)	263	93	1132	902	101	1265	41	31	2774	32	36	1926	103	92	3583	50	30	1535	72	39	2304
Hγ (4340 Å)	404	139	1120	1170	141	1217	33	31	2218	34	26	1576	70	51	2142	52	36	1313	50	31	1832
He I (4471 Å)	84	40	1032	213	33	1125	12	10	2267	3	3	960	26	24	2281	15	14	1140	9	6	1452
C III/N III (4640/4650 Å)	...	...	...	...	...	...	...	...	...	3	3	918	5	4	776	...	...	...	14	9	2521
He II (4686 Å)	27	13	1154	27	4	807	9	7	2286	15	18	960	65	73	1728	38	32	1408	16	11	2091
Hβ (4861 Å)	476	220	1125	1270	188	1111	39	37	1851	35	43	1358	95	84	2036	59	52	1542	57	47	1557
He I (4922 Å)	28	14	1011	55	8	916	...	...	...	2	3	727	10	9	1286	...	...	...	5	4	1168
He I (5016 Å)	23	13	970	59	11	978	...	...	...	...	...	...	...	...	...	...	...	...	...	...	...
He I (5875 Å)	131	89	1014	3530	70	966	13	19	1736	9	16	1481	28	32	1736	19	23	1021	21	25	1652
Hα (6563 Å)	510	341	1024	1280	287	1000	46	94	1582	40	87	1371	78	110	1599	62	81	1188	63	78	1397
He I (6678 Å)	58	54	1000	136	32	905	9	21	2205	3	8	750	6	37	1438	6	9	898	7	8	1123
He I (7065 Å)	34	40	1077	81	32	980	...	...	...	...	...	...	...	...	...	...	...	...	...	...	...

Note. Flux, EW, and FWHM are in units of 10^{-16} erg cm^{-2} s^{-1}, Å, and km s^{-1}, respectively.
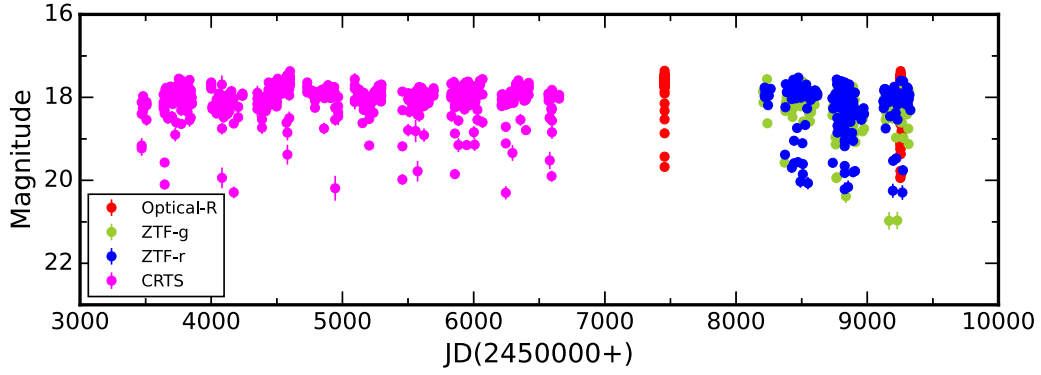
Figure 5. Combined *R*-band, ZTF-*r/g*, and CRTS light-curve variations of J0759.
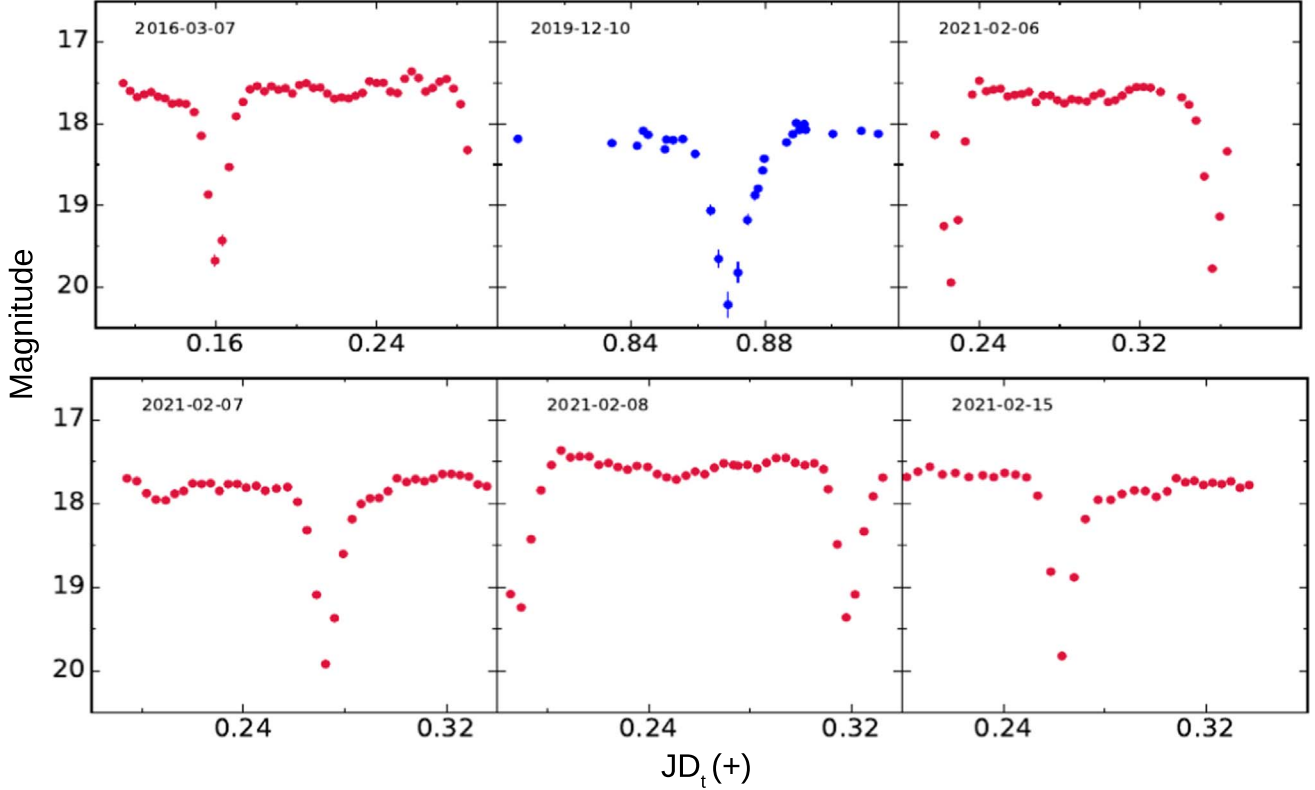
Figure 6. *R*-band (red) and ZTF-*r* (blue) light curves of J0759, where the observation day (JD$_t$) is 2,458,827.00 for the ZTF-*r*-band light curve and is given in Table 1 for photometric observations. The epochs of observation are mentioned at the top of each panel.

This estimated value of *i* is in good agreement with the values derived in terms of the graphical form of the relationship between $\Delta\phi$, *i*, and *q* for Roche geometry in Horne (1985). Considering the limiting values of WD masses in CVs, the binary separation is estimated to be in the range $(5.9-9.2) \times 10^{10}$ cm. The mean density of the secondary $\overline{\rho}$ is estimated to be 10.8 g cm^{-3}, which implies a spectral type and effective temperature of the secondary of M4.2 and 3292 K, respectively.

The total duration of an eclipse is approximately 40 minutes. This measured value of ~40 minutes is too long to represent an eclipse of just the primary star and can also be used to determine the size of the eclipsed light-producing source. Thus, we have determined the radius of the eclipsed region (*R*) by

using the following equation of Bailey (1990):

$$R = \pi a \sqrt{1 - \alpha^2} \, \Delta\phi_{\rm ie}, \qquad (4)$$

where $\Delta\phi_{\rm ie}$ is ingress/egress duration, $a = \cos i / \cos i_{\rm lim}$, *i* is the angle of inclination, and $i_{\rm lim}$ is a limiting angle of inclination for which eclipse half-width at half depth reaches zero. The average value of ingress/egress duration ($\Delta\phi_{\rm ie}$) is derived to be 0.14 ± 0.06, where the error on $\Delta\phi_{\rm ie}$ is the standard deviation of different measurements. Assuming the angle of inclination, $i \sim 78°$, the average value of $q = 0.35$, and using $i_{\rm lim}$ from Table 1 of Bailey (1990), the value of *R* is estimated to be ~ 33 $R_{\rm WD}$, where $R_{\rm WD}$ is calculated using the mass–radius relation given by Nauenberg (1972).
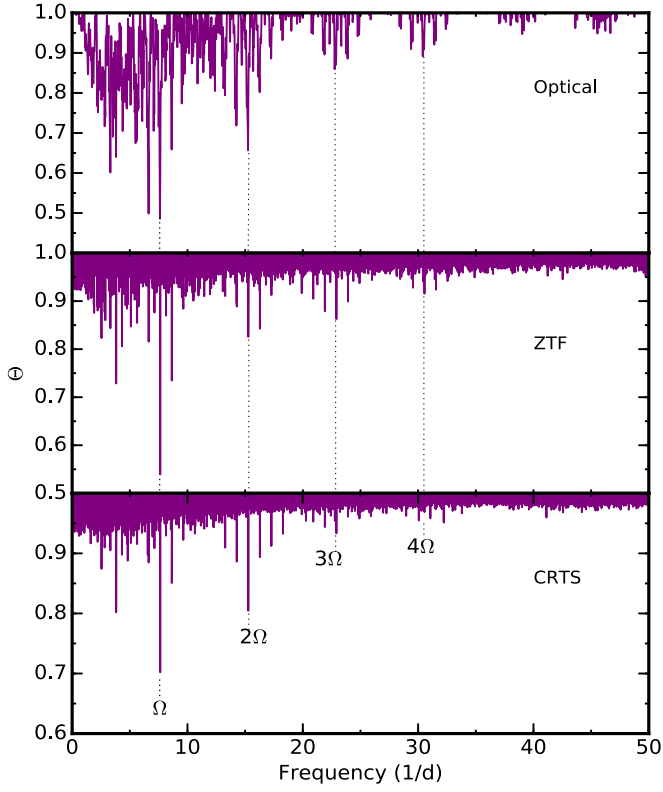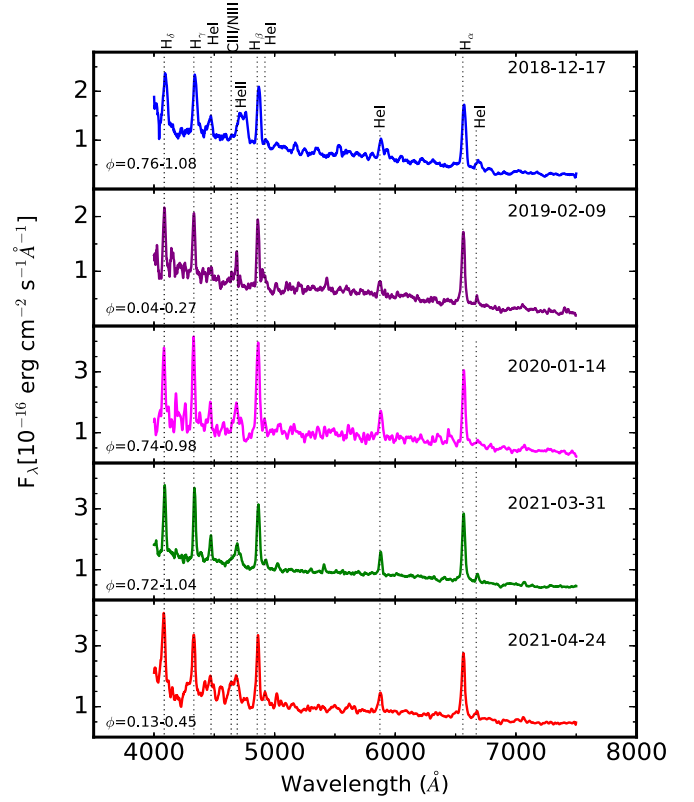
Figure 7. Top to bottom panels show the PDM periodogram of J0759 as obtained from combined *R*-band photometric, ZTF, and CRTS observations, respectively.

Figure 9. Optical spectra of J0759 for five epochs of observation. The date of observation and corresponding orbital phase are mentioned in each panel.

Table 5
Times of Minima for J0759 from *R*-band and ZTF Observations

Date of Obs.	Eclipse Minima (JD)	Cycle
2016 Mar 7	2,457,455.16058506 ± 0.00014480	0
2019 Dec 10	2,458,827.86967765 ± 0.00020655	10,484.00
2021 Feb 6	2,459,252.22568635 ± 0.00015772	13,725.00
	2,459,252.35599537 ± 0.00014890	13,725.99
2021 Feb 7	2,459,253.27295816 ± 0.00021381	13,732.99
2021 Feb 8	2,459,254.31926978 ± 0.00025254	13,740.99
2021 Feb 15	2,459,261.26253060 ± 0.00025446	13,794.01

3.2.3. Optical Spectroscopy

Optical spectra of J0759 obtained for five epochs of observation are shown in Figure 9. The orbital phase for every epoch of observation was derived using the mid-time of exposure and Equation (1). In each spectrum, we have observed strong Balmer emission lines from Hα to Hδ, along with the He I and weak He II ($\lambda 4686$) lines. We have also found weak Bowen fluorescence C III/N III emission lines in the spectra of J0759. These emission lines are found to vary from one epoch of observation to another. The current optical spectra of J0759 resemble the earlier observed optical spectrum from
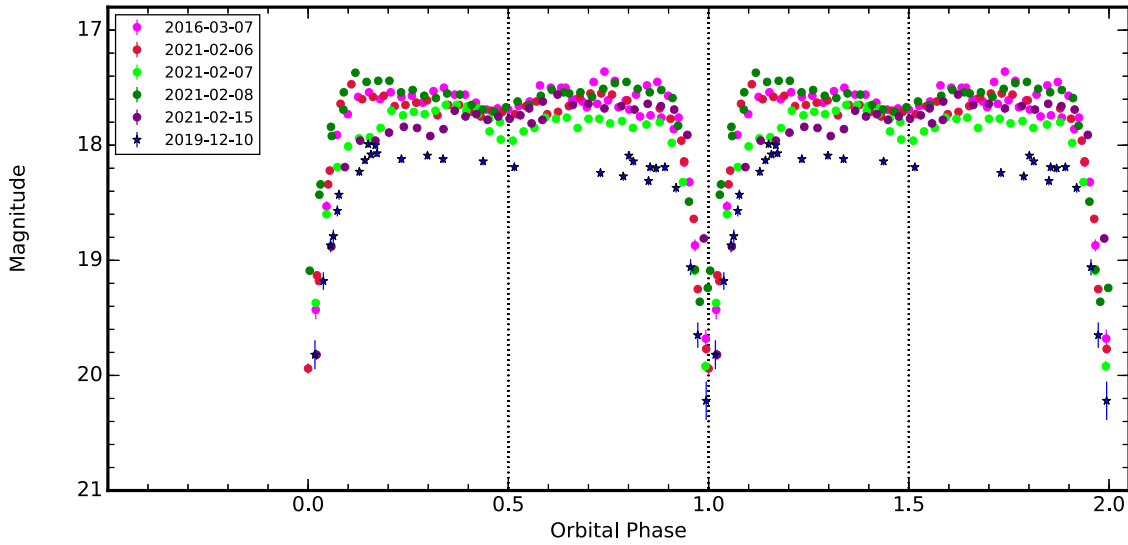
Figure 8. Orbital-phase-folded light curves of J0759 in *R* and ZTF-*r* bands.

the SDSS as obtained by Szkody et al. (2006) during the epoch 2004 November 6. The SDSS flux of the emission lines Hα, Hβ, and He I (λ4471) seems to be consistent with the observed flux for the epoch 2019 February 9; however, the He II(4686) emission line was relatively weak in the SDSS spectrum (Szkody et al. 2006).

4. Discussion

We have carried out detailed analyses of two CVs, RBS 0490 and J0759, using optical photometry and spectroscopy. We discover a photometric period of 1.689 ± 0.001 hr for RBS 0490, which is probably its orbital period. For J0759, our eclipse timings confirm and refine the previously determined period of 3.14 hr. The orbital periods of RBS 0490 and J0759 place them below and above the period gap of the orbital period distribution of CVs, respectively.

The absolute value of G-band magnitude is approximately $+9.9$ mag for RBS 0490, which appears to be similar to that for magnetic systems of AM Her type. Further, the photometric light-curve variations in RBS 0490 also look similar to a magnetic system, possibly polars, and these variations are unusual for an ordinary nova or a dwarf nova. It is interesting that these light-curve variations reveal one broad hump and then a second hump or a plateau-like structure. The main broad hump can be associated with the main accretion region. However, the observed second hump or plateau-like structure indicates that the minimum might be filled up by the emission from an independent second accretion region or may indicate accretion at a second fainter pole. Accretion onto a second pole has been seen in a few polars, e.g., in DP Leo (Cropper 1990), VV Pup (Wickramasinghe et al. 1989), UZ For (Schwope et al. 1990), and QS Tel (Schwope et al. 1995), etc. In the majority of cases, the activity from the second pole is at least one order of magnitude lower than that from the primary pole. Polarimetric observations of RBS 0490 can help to confirm the two-pole accretion in the future.

R-band light curves of J0759 exhibit deep eclipses with a depth of average magnitude ~ 2.0 mag. The observed eclipse resembles the disk rather than the highly structured eclipses often seen in AM Her stars. The absolute G-band magnitude implied by the Gaia parallax is near $+6.5$, significantly brighter than most magnetic systems. Further, the large value of eclipse radius indicates that the eclipse observed in the light curves is not solely due to the occultation of the WD by the secondary. In general, the dimension of the optical emission sites is thought to be $<0.1 \, R_{WD}$ (Bailey & Cropper 1991). Therefore, the derived large value of R indicates that the eclipse feature might be observed due to the occultation of the accretion disk and bright spot.

The optical spectra of J0759 show strong Balmer emission lines, He I, and He II along with conspicuous features of weak He II (λ4686) and Bowen fluorescence C III/N III emission lines. The weakness of He II λ4686 and the Bowen lines suggests that J0759 is not a magnetic CV (Warner 1995). However, this is not a sufficient criterion for a CV classification. More specifically, the ratio of EW[He II (λ4686)/Hβ] and EW of the Hβ emission line provides a criterion to separate magnetic CVs from nonmagnetic CVs (Silber et al. 1992). According to Silber's criteria, magnetic CVs are characterized by the ratio EW[He II (λ4686)/Hβ] $\geqslant 0.4$ and Hβ $\geqslant 20$ Å. For J0759, we have detected Hβ $\geqslant 20$ Å for all observations; however, the EW ratio of He II (λ4686) to Hβ is not found

to be more than 0.4 for all epochs of observation. For the epochs 2018 December 17 and 2021 April 24, we have observed this ratio is close to 0.2, which is not quite up to the values for magnetic CVs. The Balmer decrement can also be used in order to distinguish the magnetic and nonmagnetic nature of the system. The inverted Balmer decrement is possibly present in the low-state spectra of the AM Her type of magnetic CVs. However, a flat Balmer decrement, implying that the Balmer emission lines are optically thick, has been observed in most of the nonmagnetic CVs and also in intermediate polars (Warner 1995). For J0759, a flat Balmer decrement is observed in most epochs of observation. Cyclotron hump features are also not detected in the optical spectra of J0759. Thus, it appears that the system J0759 satisfies the majority of the criteria for being nonmagnetic, but further observations are needed for definitive classification.

In the case of RBS 0490, optical spectra also consist of strong emission lines of the Balmer series and He I together with the weak emission line of He II (λ4686). The presence of single-peaked strong Balmer emission lines and the large equivalent width of the Hβ emission line may imply a magnetic CV classification for this system. However, other possible factors like weak He II (λ4686), broad Balmer emission lines, the observed flat Balmer decrement, the ratio of EW[He II (λ4686)/Hβ] ~ 0.1 and 0.02 (for epochs 2017 December 22 and 2018 November 30), and the nondetection of a cyclotron hump in the optical spectrum either weaken its chance to be magnetic or may imply the low magnetic strength of the WD. A low magnetic field strength of the WD was also proposed by Harrison & Campbell (2015) from the combined WISE and JHK observations of RBS 0490.

5. Conclusions

We have presented optical photometric and spectroscopic observations of RBS 0490 and J0759 that lead us to the following conclusions.

1. RBS 0490 has been found to vary with a period of 1.689 ± 0.001 hr, which was not evident in earlier studies and can be interpreted as its orbital period. The probable orbital period places it below the period gap of the orbital period distribution of CVs. The variability observed in RBS 0490 seems to favor magnetic systems, possibly polars, and provide evidence of emission from an independent second accretion region or a second fainter pole. However, the characteristic features seen in the optical spectra of RBS 0490 either weaken its chance to be magnetic or may imply the low magnetic strength of the WD.

2. Our eclipse photometry confirms and refines the ~ 3.14 hr period of J0759, placing it longward of the period gap. The eclipses are consistent with a disk and an orbital inclination of $\sim 78°$. The detection of strong Balmer emission lines along with the weak high-ionization emission lines hints toward the nonmagnetic nature of J0759.

ORCID iDs

Arti Joshi ● https://orcid.org/0000-0001-9275-0287
Wei Wang ● https://orcid.org/0000-0003-3901-8403

References

Andronov, I. L., & Andrych, K. D. 2014, OAP, 27, 38
Bailey, J. 1990, MNRAS, 243, 57
Bailey, J., & Cropper, M. 1991, MNRAS, 253, 27
Beardmore, A. P., Ramsay, G., Osborne, J. P., et al. 1995, MNRAS, 273, 742
Bellm, E., Kulkarni, S., & Graham, M. 2019, AAS Meeting Abstracts, 233, 363.08
Beuermann, K., Baraffe, I., Kolb, U., & Weichhold, M. 1998, A&A, 339, 518
Bridge, C. M., Cropper, M., Ramsay, G., et al. 2003, MNRAS, 341, 863
Cropper, M. 1990, SSRv, 54, 195
Dekany, R., Smith, R. M., Riddle, R., et al. 2020, PASP, 132, 038001
Drake, A. J., Djorgovski, S. G., Mahabal, A., et al. 2009, ApJ, 696, 870
Drake, A. J., Gänsicke, B. T., Djorgovski, S. G., et al. 2014, MNRAS, 441, 1186
Eggleton, P. P. 1983, ApJ, 268, 368
Gaia Collaboration, Brown, A. G. A., Vallenari, A., et al. 2021, A&A, 650, C3
Gänsicke, B. T., & Dillon, M. 2009, MNRAS, 397, 2170
Graham, M. J., Kulkarni, S. R., Bellm, E. C., et al. 2019, PASP, 131, 078001
Harrison, T. E., & Campbell, R. K. 2015, ApJS, 219, 32
Horne, J. H., & Baliunas, S. L. 1986, ApJ, 302, 757
Horne, K. 1985, MNRAS, 213, 129
Knigge, C. 2006, MNRAS, 373, 484
Lomb, N. R. 1976, Ap&SS, 39, 447
Mason, P. A., Ramsay, G., Andronov, I., et al. 1998, MNRAS, 295, 511
Nauenberg, M. 1972, ApJ, 175, 417
Patterson, J. 1994, PASP, 106, 209
Prabhu, T. P., & Anupama, G. C. 2010, in ASI Conf. Ser. 1, Interstellar Matter and Star Formation: A Multi-wavelength Perspective, ed. D. K. Ojha (New Delhi: ASI), 193
Ricker, G. R., Winn, J. N., Vanderspek, R., et al. 2015, JATIS, 1, 014003
Rosen, S. R., Mittaz, J. P. D., Buckley, D. A., et al. 1996, MNRAS, 280, 1121
Sagar, R., Omar, A., Kumar, B., et al. 2011, CSci, 101, 1020
Salvi, N., Ramsay, G., Cropper, M., Buckley, D. A. H., & Stobie, R. S. 2002, MNRAS, 331, 488
Scargle, J. D. 1982, ApJ, 263, 835
Scaringi, S., Bird, A. J., Norton, A. J., et al. 2010, MNRAS, 401, 2207
Schmidt, G. D., Hoard, D. W., Szkody, P., et al. 1999, ApJ, 525, 407
Schwope, A. D., Beuermann, K., & Thomas, H.-C. 1990, A&A, 230, 120
Schwope, A. D., Brunner, H., Buckley, D., et al. 2002, A&A, 396, 895
Schwope, A. D., Thomas, H. C., & Beuermann, K. 1993, A&A, 271, L25
Schwope, A. D., Thomas, H. C., Beuermann, K., et al. 1995, A&A, 293, 764
Silber, A., Bradt, H. V., Ishida, M., Ohashi, T., & Remillard, R. A. 1992, ApJ, 389, 704
Sinvhal, S. D., Kandpal, C. D., Mahra, H. S., Joshi, S. C., & Srivastava, J. B. 1972, in Optical Astronomy with Moderate Size Telescopes, ed. R. V. Karandikar et al. (Hyderabad: Osmania Univ.), 64
Smith, D. A., & Dhillon, V. S. 1998, MNRAS, 301, 767
Stellingwerf, R. F. 1978, ApJ, 224, 953
Szkody, P., Henden, A., Agüeros, M., et al. 2006, AJ, 131, 973
Thorstensen, J. R., Lépine, S., & Shara, M. 2006, PASP, 118, 1238
Voges, W., Aschenbach, B., Boller, T., et al. 1999, A&A, 349, 389
Warner, B. 1986, MNRAS, 219, 347
Warner, B. 1995, CAS, 28, 146
Wickramasinghe, D. T., Ferrario, L., & Bailey, J. 1989, ApJL, 342, L35
Zorotovic, M., Schreiber, M. R., & Gänsicke, B. T. 2011, A&A, 536, A42